A one dimensional model for ion transport in a flame with two absorbing surfaces

Christopher Martin[a], Alexandrina Untaroiu[b], and Kemu Xu[b]

[a]Penn State University, Altoona PA; [b]Virginia Tech, Blacksburg, VA

ARTICLE HISTORY
Compiled September 18, 2020

ABSTRACT
This paper presents numerical and asymptotic analytical solutions for the current-voltage characteristic of a flame using a one-dimensional ion transport model with boundary conditions that include detailed treatment of sheath formation. Nondimensional conservation equations are presented for the free electron, the hydronium ion, and the electrical potential in a one-dimensional flow field with uniform velocity, electrical mobility, and diffusivity, but allowances are made for non-equilibrium electron temperature. In this study, the size and location of the ion formation region and the electric Reynolds numbers are changed, and their impacts are studied. The model predicts the formation of charged sheaths at both ends of the domain, which are responsible for saturation events that are reliably observed in experiments. A new saturation regime can be made to appear in the model, but its absence from experiment is argued to have implications on transport near absorbing surfaces in the experiment. For example, the Reynolds numbers at which the current-voltage characteristic converges to the shape and magnitude observed in experiment implies that the sheaths form in low-velocity region in the real flow that reduce the apparent Reynolds number.

Corresponding Author, C. Martin Email: crm28@psu.edu

Nomenclature

Dimensioned		
D_k	Diffusivity spec. k	$\mathrm{m^2 s^{-1}}$
e	Fundamental charge (1.6E-19)	C
k_b	Boltzmann const. (1.38E-23)	$\mathrm{J\ K^{-1}}$
k_r	Recombination coef.	$\mathrm{s^{-1} m^3}$
L	Domain length	m
n_k	Num. dens. of spec. k	$\mathrm{m^{-3}}$
n_0	Ion density scale	$\mathrm{m^{-3}}$
p	Pressure	Pa
q_k	Charge of species k	C
T_k	Temperature of spec. k	K
U	Total bulk velocity	$\mathrm{m\,s^{-1}}$
Γ	Number flux density	$\mathrm{s^{-1}\ m^{-2}}$
λ_d	Debye length	m
λ_r	Recombination length	m
ε_0	Vac. permittivity (8.9E-12)	$\mathrm{C\ V^{-1}\ m^{-1}}$
μ_k	Mobility of spec. k	$\mathrm{m\,N^{-1} s^{-1}}$
ρ	Mass density	$\mathrm{kg\,m^{-3}}$
$\dot{\omega}_f'''$	Vol. ion formation rate	$\mathrm{s^{-1} m^{-3}}$
Dimensionless		
R_k	Reynolds num. of spec. k	$UL/\mu_k k_b T_i$
K_z	Sheath thickness coef.	$\sqrt{2\alpha^2 {\eta_s}^{-1}}$
z	D'less position	x/L
z_1	Formation regn. start	
z_2	Formation regn. end	
L_f	Formation regn. width	$z_2 - z_1$
α	Debye length	λ_d/L
β	Recombination rate	$k_r n_0 L/U$
η	Positive ion density	n_i/n_0
η_{d1}	Downstream sheath ion dens.	
η_s	Upstream sheath ion dens.	${R_i}^{1/2}\alpha\dot{\omega}^{1/2}\tau^{-1/2}$
η_2	Peak ion density	
η_∞	Inf. len. ion density	
ν	Negative ion density	n_e/n_0
ϕ	Electric potential	$Ve/k_b T_e$
ϕ_p	Plasma potential	
ϕ_a	Applied potential	
τ	Elec./ion temp. ratio	T_e/T_i
$\dot{\omega}$	D'less formation rate	$\dot{\omega}_f''' L/U n_0$

1. Introduction

This paper presents a one-dimensional reduced-order model for the transport of ions between two absorbing surfaces in a flame. The purpose of the effort is to identify links between aspects of the flame's small-signal voltage-current characteristic and transport mechanics and boundary conditions. To formulate a problem that permits an anlytical solution for these features, we drastically simplify the geometric and chemical kinetic

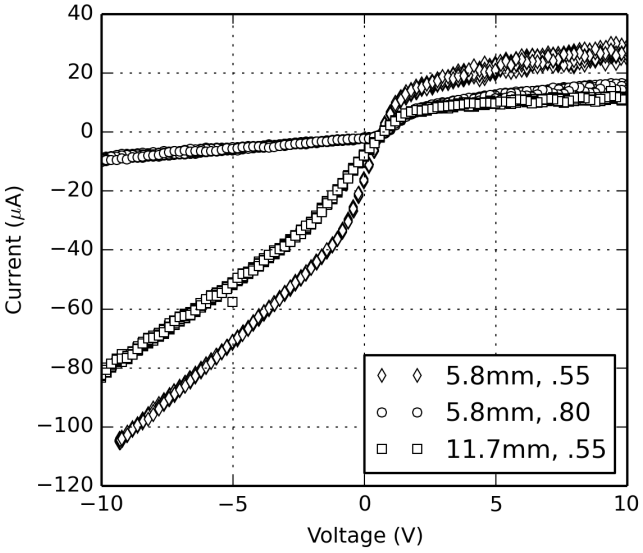

Figure 1. Current-voltage characteristics for three combinations of standoff distance and fuel/oxygen ratio by volume.

complexity of the problem in favor of a detailed treatment of metal surfaces' sheaths. The work demonstrates that even in the absence of detailed numerical simulation, by taking pains to model these compact regions of charge at metal surfaces, the model correctly predicts the important features of the current-voltage (IV) characteristic.

The work is originally inspired by a series of experimental investigations into the electrical aspects of the oxyfuel cutting torch [21, 22, 25, 23], but it is sufficiently abstracted that it might apply to a number of flame geometries. The oxyfuel cutting torch flame is formed by an annular array of circular jets of premixed fuel and oxygen gas. The jets vary in number and size, but the entire flow regime is typically on the order 6mm (1/4-inch) in diameter. These jets form an array of bunsen-like inner cones, about 4mm (0.16in) in length, in which Hydronium (H_3O^+) and free electron (e^-) are the most numerous charged species. The products of the inner cones converge to form a single faintly luminous outer-cone, where the charged species recombine before impacting the work piece. The flame and the experiment are described in more detail in the above sources.

In its typical use, the oxyfuel torch is held over some metal work piece, which the flame is used to heat. When an electrical potential in the range $\pm$10V is applied between the torch tip and the work piece, IV characteristics can be measured like those shown in Figure 1 (taken from [21]). The authors identify three regimes of the IV characteristic, each with an apparently piece-wise linear behavior: (from left to right) regimes 1 and 2 are locally linear; regime 3 is *saturated*. The authors demonstrate empirical relationships to the flow and process parameters [22, 25].

There is a multitude of similar efforts intended to leverage ion currents for sensing in propulsion systems [7, 24, 19], IC engines [14, 26, 27], mass spectroscopy [15], and especially furnaces and boilers [16, 34, 6]. In most of these applications, it is sufficient to detect the presence, absence, or timing of ion current signals, while it is comparatively rare to leverage the details of calibrated IV characteristics as a sensing technique.

In comparison to the number of works examining ionic winds and their impact on

flame stability, burning velocity, or chemical kinetic studies (e.g. [20, 33, 2, 32, 3]), there are relatively few works that scrutinize the small-signal characteristics of ion currents in flames with significant geometric complexity.

Speelman et al. and Han et al. both conducted numerical studies with detailed transport and reduced chemistry on one-dimensional burner-stabilized flames with a downstream absorbing surface. Both predicted saturation and some piece-wise characteristics with interesting similarities to those observed in the oxyfuel flame [30, 29, 13]. Xiong et al. used a highly simplified model much more in the spirit of the present work to examine small signal currents in counter-flow flames, and also identified piece-wise behaviors [35]. Yamashita used detailed chemical and transport models to study the IV characteristics of a bluff-body anchored flame [36]. Meanwhile, Di Renzo et al. modeled IV characteristics of a diffusion flame using a flamelet progress variable approach, and they predicted that minority negative species can have measurable impacts on flame voltage distributions [28].

These works offer several common themes with relevance to the present endeavor. Firstly, saturation is known to occur when regions of the fluid are diminished of one or more charge carriers, so further intensifying the electric field has little or no effect on the current. The piece-wise behaviors can be made to occur when ions are transported to or evacuated from regions in space bridging absorbing surfaces and regions where charged species are formed. The strong asymmetry between electron and Hydronium mobilities causes similar asymmetry in the positive versus the negative portion of the IV characteristic.

The present work takes a fundamentally different approach. All of the works listed above as pertaining to small signal characteristics used boundary conditions that permit non-zero ion concentrations at absorbing surfaces. While that assumption can be a reasonable simplification for convergence in full-scale numerical modeling, the tiny charged sheaths that form around absorbing surfaces in plasmas were shown a century ago to cause many of the nonlinear aspects of the voltage-current characteristics in flames and plasmas [18, 4, 1]. They are frequently neglected in high-voltage studies because their effects are small compared to the applied potentials, but when considering small-signal measurements, they are quite important.

Sometimes called the Langmuir sheath, these charged regions occur naturally (without the application of external electric fields) near surfaces with zero ion density boundary conditions (metal or absorbing surfaces) due to the severe imbalance in charge carrier mobility [31, 8]. Hydronium and the free electron differ in mass by a factor of about 35,000, so their transport properties are so asymmetrical that absorbing metal surfaces depleat the negative charge around them, leaving only a thin film of positive charge, called a sheath. This can mimic the semi-conductor characteristics of metal oxide semiconductors, and they occur on scales that can be thousands of times smaller than the domain.

Descriptions of sheaths in flames feature prominently in Fialkov's review [12], Langmuir probe studies were an essential part of the early identification of ions [5], and measurements in flames were even among the first confirming the sheath's existence [4]. More recently, Karrer et al. used escalating voltages to grow a sheath through the non-reacting gap at the edge of a flame propagating along a wall as a means of measuring the quenching distance [17]. Perhaps the most complete work on theory of sheath formation in dense flowing plasmas is due to Clements and Smy's studies of Langmuir probes in flames [8, 10, 9, 11].

With the philosophy that analytical links between fundamental physics and IV characteristics are to be valued above precise numerical predictions, we deliberately

abandon all but the most essential physics. We presume that regions where ions are formed is known a priori and that the essential effects of transport can be reasonably approximated as uniform in a single dimension. Further, the derivation presumes that the applied electric fields are too feeble to impact the bulk flow.

This work presumes that the system is in a regime where the physical domain size, L, the Debye length, λ_d, and the mean-free-path, λ, are sized $L \gg \lambda_d \gg \lambda$. As was commented by Fialkov in his review of the topic [12, pp.406], the plasma found in flames is in a regime uncommon to much of the study of plasmas, which has tended to focus on the very sparse and the very hot ($T > 10^4$K), where this order might be reversed entirely.

2. Model

2.1. Derivation

In a dense flowing plasma, the number flux density, Γ_k, of a charged species, k, subjected to convection, diffusion, and electrical body forces, is

$$\Gamma_k = U n_k - D_k \frac{\mathrm{d}n_k}{\mathrm{d}x} - \mu_k q_k n_k \frac{\mathrm{d}V}{\mathrm{d}x}. \tag{1}$$

For clarity, it should be emphasized that instead of mobility, μ_k, many authors work in terms of *electrical mobility*, which is treated here as $\mu_k q_k$ with units $\mathrm{m^2V^{-1}s^{-1}}$.

When the same species is formed at a rate, $\dot{\omega}_f'''$, and is annihilated by a recombination reaction, it obeys the conservation equation,

$$0 = -\frac{\mathrm{d}\Gamma_k}{\mathrm{d}x} + \dot{\omega}_f''' - k_r n_i n_e. \tag{2}$$

This equation presumes that there are only two oppositely charged species, n_e and n_i (electron and ion respectively) that recombine with some rate coefficient, k_r.

At this juncture, the derivation benefits from the Einstein relation, $D_k = \mu_k k_b T_k$, and the generous simplifying assumption that neither the transport coefficients nor temperatures have spatial derivatives. After substitution, the result is a generalized conservation equation in one dimension,

$$0 = -U\frac{\mathrm{d}n_k}{\mathrm{d}x} + \mu_k k_b T_k \frac{\mathrm{d}^2 n_k}{\mathrm{d}x^2} + \mu_k q_k \frac{\mathrm{d}}{\mathrm{d}x}\left(n_k \frac{\mathrm{d}V}{\mathrm{d}x}\right) + \dot{\omega}_f''' - k_r n_i n_e. \tag{3}$$

This equation may be written twice: once for the free electron, n_e, and once for the positive ion, n_i.

Meanwhile, the Poisson equation governs the voltage field, V, response to space charge.

$$\frac{\mathrm{d}^2 V}{\mathrm{d}x^2} = \frac{e}{\varepsilon_0}(n_e - n_i) \tag{4}$$

Here, n_e and n_i are the number densities of the free electron and the positive ion. The fundamental charge, e, and vacuum permittivity, ε_0, are defined in the nomenclature.

2.2. Boundary conditions

The domain may be defined over a range $x \in [0, L]$, such that the torch issuing the reacting fluid is imagined to be at $x = 0$, and a work piece is imagined to be at $x = L$. This places the velocity in the positive direction, so U will be positive.

Both the torch tip and the work piece are absorbing surfaces, so the number density boundary conditions are all the same,

$$n_e(0) = n_e(L) = n_i(0) = n_i(L) = 0.$$

Some voltage, V_a, may be imposed at the torch, while the work piece is imagined to be at ground potential. Therefore,

$$V(0) = V_a \qquad\qquad V(L) = 0$$

2.3. Nondimensionalization

The domain offers a natural length scale, L, and the ions are known to occur in some density, n_0. Other scales are offered naturally by the governing equations, including the electric potential due to thermal motions $k_b T_e/e$. We adopt nondimensional variables,

$$z = \frac{x}{L} \qquad \eta = \frac{n_i}{n_0} \qquad \nu = \frac{n_e}{n_0} \qquad \phi = \frac{Ve}{k_b T_e}.$$

The new length scale and the ion concentration scales are such that $z, \eta, \nu \in [0, 1]$.

The voltage has been nondimensionalized by the "thermal" kinetic energy, $k_b T_e$, the electrical energy needed for electrical motion to begin to dominate natural diffusive processes. In a 3,000K flame, $\phi = 1$ corresponds to about 0.26V, so large values of ϕ may be considered. We have taken some pains to emphasize, however, that this work will consider only "small" applied voltages. We define a limit for this assumption by asserting that the electrical body do not contribute significantly to the fluid's bulk kinetic energy,

$$\left| \frac{2n_0 e V_a}{\rho U^2} \right| \ll 1. \tag{5}$$

If the velocity is 75m/s, ion density on the order $5 \times 10^{17}\text{m}^{-3}$, and bulk density on the order 0.1kg m^{-3}, then an applied voltage around 3.5kV is necessary to violate this assumption. We may establish a similar limit on ϕ as the ratio of bulk kinetic to ion thermal energy density,

$$|\phi_a| \ll \frac{\rho U^2}{2n_0 k_b T}. \tag{6}$$

Under the same physical conditions, the applied dimensionless potential, $\|\phi_a\|$, must be smaller than 13,500.

When these terms are substituted, and the conservation equations are normalized

by the convection scale, $n_0 U/L$,

$$0 = -\eta' + R_i{}^{-1}[\eta'' + \tau(\eta\phi')'] + \dot{\omega} - \beta\eta\nu \tag{7a}$$

$$0 = -\nu' + R_e{}^{-1}[\nu'' - (\nu\phi')'] + \dot{\omega} - \beta\eta\nu \tag{7b}$$

$$\alpha^2\phi'' = \nu - \eta. \tag{7c}$$

This introduces a number of important dimensionless groups.

$$R_k = \frac{UL}{\mu_k k_b T_k} \qquad \dot{\omega} = \frac{\dot{\omega}_f''' L}{U n_0} \qquad \alpha = \sqrt{\frac{\varepsilon_0 k_b T_e}{e^2 n_0 L^2}} = \frac{\lambda_d}{L}$$

$$\beta = \frac{k_r n_0 L}{U} = \frac{L}{\lambda_r} \qquad \tau = \frac{T_e}{T_i}$$

The ionic and electric Reynolds numbers, R_i and R_e, are the ratios of convective transport to diffusive and electrical transport for the ion and the free electron respectively. The dimensionless formation rate, $\dot{\omega}$, is the ratio of formation to convection. A unity value for ω over the entire domain would result in unity η and ν if diffusion and recombination are neglected. The dimensionless Debye scale, α, is the ratio of the Debye length to the domain length. The recombination strength, β, is the inverse of a nondimensionalization of the recombination length scale, $\lambda_r = U/k_r n_0$. The recombination length is the distance over which the recombination reaction occurs in the convecting flow. Finally, the temperature ratio, τ, is the ratio of the electron temperature to the ion temperature. Typically, the ion temperature is quite close to the bulk flow temperature, but electrons' tendency to retain thermal energy often leads them to higher, non-equilibrium temperatures.

The boundary conditions become

$$\eta(0) = \eta(1) = \nu(0) = \nu(1) = 0$$

$$\phi(0) = \phi_a \qquad \phi(1) = 0.$$

Using the same approach to the total current and the number flux densities,

$$F_i = \frac{\Gamma_i}{U n_0} = \eta + R_i{}^{-1}[-\eta' - \tau(\eta\phi')] \tag{8a}$$

$$F_e = \frac{\Gamma_e}{U n_0} = \nu + R_e{}^{-1}[-\nu' + (\nu\phi')] \tag{8b}$$

$$J = \frac{I}{U n_0 e} = F_i - F_e \tag{8c}$$

2.4. Selection of $\dot{\omega}$

The dimensionless formation rate, $\dot{\omega}$, is presumed to occur in a known region, and we will further presume that it is uniform over this region. The physical ion formation rate, $\dot{\omega}_f'''$, is difficult to determine explicitly from experiment, but ion densities have been

measured explicitly, so it is much more sound to construct the nondimensionalization scheme around n_0 rather than $\dot{\omega}_f'''$.

The true relationship between ion density and formation rate is a balance between transport, formation, and recombination, but when convection is presumed to dominate the other processes, this relationship is quite simple. Consider a model limited to a uniform region of ion formation between z locations, z_1 and z_2, and zero everywhere else. When convection dominates, η' and ν' are equal to $\dot{\omega}$, so to enforce that η and ν are on the order 1,

$$\dot{\omega} = \begin{cases} \frac{1}{z_2 - z_1} & : \quad z_1 < z < z_2 \\ 0 & : \quad \text{otherwise.} \end{cases} \tag{9}$$

The actual solution for the peak values of η and ν will not be precisely one, but they will not deviate too far from unity so long as the assumption that convection is strong remains true. Fortunately, this will have little bearing on the model results; it is merely a choice of nondimensionalization scheme.

2.5. Perturbation

The appearance of piece-wise linear behaviors in the IV characteristics inspires special treatment for the effect changes in voltage have on the solution. If the $\phi(0)$ boundary condition is modified to be

$$\phi(0) = \phi_a + \epsilon, \tag{10}$$

where ϵ is the perturbation in the applied potential, the resulting solution may be written as a polynomial expansion on ϵ.

$$\eta = \eta_0 + \epsilon\eta_1 + \epsilon^2\eta_2 + \ldots \qquad \nu = \nu_0 + \epsilon\nu_1 + \epsilon^2\nu_2 + \ldots$$
$$\phi = \phi_0 + \epsilon\phi_1 + \epsilon^2\phi_2 + \ldots \qquad J = J_0 + \epsilon J_1 + \epsilon^2 J_2 + \ldots$$

When these perturbed values are substituted into (7a), (7b), and (7c), the results are polynomials on ϵ, where each coefficient of ϵ is an independent differential equation. The constant-term is merely identical to the original equations, and may be discarded as redundant. The coefficient of ϵ provides the linearized response to perturbations in applied voltage:

$$0 = -\eta_1' + {R_i}^{-1}[\eta_1'' + \tau(\eta_0\phi_1')' + \tau(\eta_1\phi_0')'] - \beta(\eta_0\nu_1 + \eta_1\nu_0) \tag{11a}$$
$$0 = -\nu_1' + {R_e}^{-1}[\nu_1'' - (\nu_0\phi_1')' - (\nu_1\phi_0')'] - \beta(\eta_0\nu_1 + \eta_1\nu_0) \tag{11b}$$
$$\alpha^2\phi_1'' = \nu_1 - \eta_1. \tag{11c}$$

The boundary conditions are

$$\eta_1(0) = \eta_1(1) = \nu_1(0) = \nu_1(1) = 0$$

$$\phi_1(0) = 1 \qquad \phi_1(1) = 0$$

Table 1. Conditions for the five cases modeled in the present study.

	R_i	α	β	τ	z_1	z_2
Case 1	1,000	10^{-3}	20	1	.01	.21
Case 2	2,000	10^{-3}	20	1	.01	.21
Case 3	1,000	10^{-3}	20	1	.00	.20
Case 4	2,000	10^{-3}	20	1	.00	.20
Case 5	1,000	10^{-3}	20	1	.00	.40

Finally, the flux and current densities are

$$F_{i,1} = \eta_1 + {R_i}^{-1}[-\eta_1' - \tau(\eta_0\phi_1') - \tau(\eta_1\phi_0')] \tag{12a}$$

$$F_{e,1} = \nu_1 + {R_e}^{-1}[-\nu_1' + (\nu_0\phi_1') + (\nu_1\phi_0')] \tag{12b}$$

$$J_1 = F_{i,1} - F_{e,1}.. \tag{12c}$$

3. Asymptotic Analysis

The governing equations, (7a), (7b), and (7c), were discretized using a method of finite differences with quadratic interpolation in a non-uniform grid. Sheaths at the up-stream and down-stream boundaries caused intense gradients, requiring a high density of nodes that was not necessary in the center of the solution. Once discretized, the problem was reduced to a quadratic tensor problem on a solution vector, x, containing node values for η, ν, and ϕ. This was then solved using Newton iteration. On convergence, the residuals from (7a), (7b), and (7c) were on the order 10^{-10}.

3.1. Selection of Parameters

There are five cases represented here, and in each all conditions were held constant while varying the applied dimensionless potential, ϕ_a, from -50 to +40. In a 3000K flame, this corresponds roughly to -12 to 10V. The ionic Reynolds number, R_i, and the start, z_1, and end, z_2, of the formation region were varied while values for α, β, and τ were held constant. Note that the size of the reaction region (and $\dot{\omega}$) were held constant in all but case 5.

These conditions are intended to be crudely representative of those observed in the oxyfuel preheat flame. The physical domain is approximately 12mm (.5in) long, and the inner cone flame length is readily observed to be about 2.4mm (0.1in) long. The lifted conditions represent a 0.1mm gap between the flame and the torch tip. If the velocity is about 75m/s, ion density scale, n_0, is on the order $5 \times 10^{17}\mathrm{m}^{-3}$, and recombination rate coefficient, k_r, is $2.4 \times 10^{-13}\mathrm{m}^3/\mathrm{s}$ (as used by [12, 2, 30]) the dimensionless recombination scale, β, is on the order 20. The Debye length in such a plasma at a temperature 3000K can be calculated to be on the order of 10μm, so α is determined to be on the order of 1/1000 of the domain length.

The Reynolds number of such a plasma is likely to be on the order 3,000 or higher in the bulk of the flame, where velocity is at its maximum. Instead, we have elected to examine cases with lower Reynolds numbers to reflect the conditions near the absorbing surfaces. The result of this choice will be clear in Section 4, and the implications of these results are specifically addressed in the conclusions.

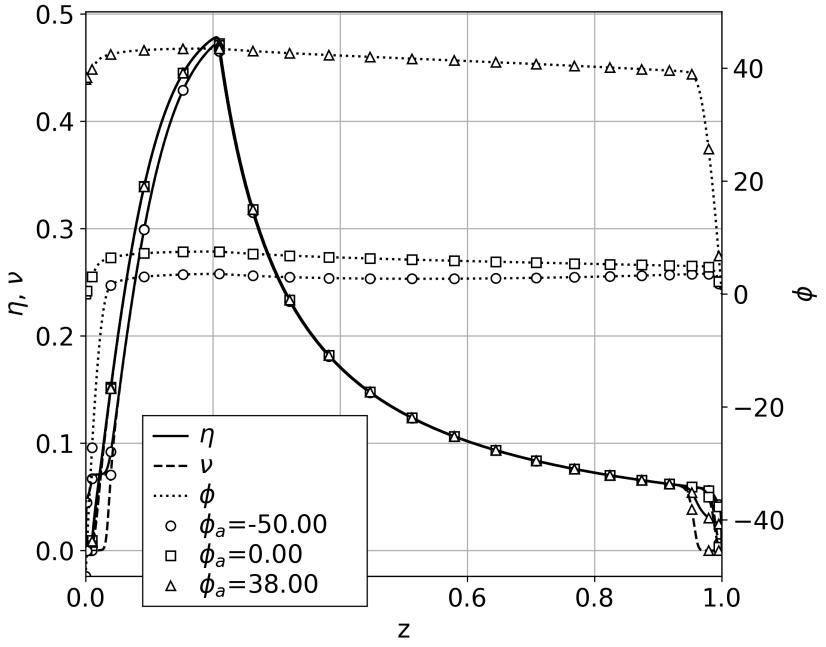

Figure 2. Three solutions selected from case 2. ϕ should be read from the right-hand axis. η and ν should be read from the left-hand axis.

3.2. Numerical Solution

Figure 2 shows numerical solutions for three applied potentials, $\phi(z = 0) = \phi_a$, selected from case 2. The dimensionless hydronium and electron concentrations, η and ν, are shown with solid and dashed lines respectively. Two of the conditions give results precisely on top of one another, but applying a negative potential has the counter-intuitive effect of shifting the ion concentrations right slightly. Otherwise, the ion concentrations predictably rise in the formation region and decline in the downstream region due to recombination.

It is clear from these solutions that the bulk of the interesting physics occurs in the small charged sheaths that form near the $z = 0$ and $z = 1$ boundaries. These form when the imbalance in mobility of the two charge carriers causes one to deplete (usually the more mobile electron) while the other lingers. The charge creates a region of intense electric field, which elevates the plasma potential from ground (usually smaller than order 10). Classically, the plasma potential is regarded as zero, but since this system already has a well defined reference potential, we will call this ϕ_p.

3.3. Upstream Sheath

Figure 3 shows the upstream sheath (near $z = 0$) more clearly. As will become clear in the next section, the downstream sheath is always present, but, as can be seen here, the upstream sheath only exists when the applied potential is sufficiently strong to grow the region of positive charge. The electron mobility is so much greater than hydronium that the same potential completely evacuates the region of electrons, so all currents there are due to positive ions.

Setting ν to zero everywhere in (7a) and (7c) so drastically simplifies the system

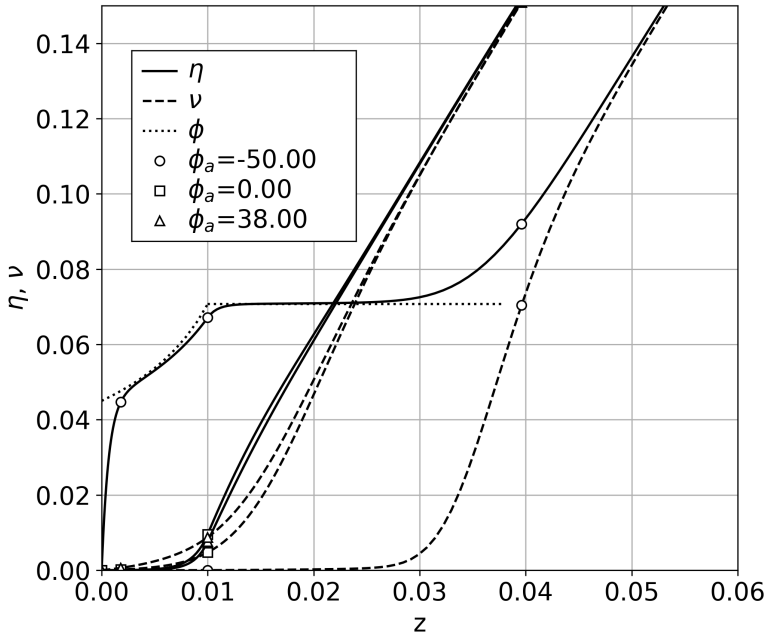

Figure 3. The sheaths at $z = 0$ from Figure 2. The dotted line has been repurposed to represent the asymptotic solution for the only saturated case shown.

that it becomes possible to derive an asymptotic solution. These can be combined to yield

$$0 = \alpha^2\phi''' - {R_i}^{-1}\alpha^2\phi'''' - \tau{R_i}^{-1}\alpha^2(\phi''\phi')' + \dot{\omega}. \tag{13a}$$

$$\eta = -\alpha^2\phi'' \tag{13b}$$

Next, the solution must be divided into two sections in space; one upstream of the formation region, $z < z_1$, where the formation rate is zero, and one downstream of that, where $\dot{\omega}$ is constant. The sheath will then extend to a location, z_s, at which point the electron concentration abruptly rises and the electric potential relaxes into the plasma potential. This sheath thickness must be greater than the flame offset, z_1. Were that not the case, then there would be no conductive layer of ions, and there would be no saturation current.

The boundary conditions on these piece-wise solutions are

$$\begin{array}{ccc} \phi(0) = \phi_a & \phi(z_s) = \phi_p & \phi'(z_s) \approx 0 \\ \phi({z_1}^+) = \phi({z_1}^-) = \phi_1 & \phi'({z_1}^+) = \phi'({z_1}^-) & \eta({z_1}^+) = \eta({z_1}^-) \end{array}$$

This implies the definition of three important parameters: ϕ_1, the interface potential between the two regions, z_s, the sheath thickness, and ϕ_p, the plasma potential above ground. These conditions also include the assumption that the field strength (ϕ') away from the sheath is small.

Equation (13a) may be twice integrated to obtain

$$-\frac{\dot{\omega}}{2\alpha^2}z^2 + C_1 z + C_0 = \phi' - {R_i}^{-1}\phi'' - \tau {R_i}^{-1}\frac{1}{2}(\phi')^2 \tag{14}$$

where C_1 and C_0 are integration constants.

In the region where $\dot{\omega}$ is not zero, this is solved precisely by a quadratic on z, so after applying the above boundary conditions, when $z_1 < z < z_s$,

$$\phi(z) = -\frac{\eta_s}{2\alpha^2}(z_s - z)^2 + \phi_p \tag{15a}$$

$$\eta(z) = \eta_s = \sqrt{\frac{R\alpha^2\dot{\omega}}{\tau}} = \text{const.} \tag{15b}$$

It should be emphasized that while the ion concentration can already be solved explicitly, the sheath thickness, z_s, is still unconstrained. However, it can be seen by evaluating (15a) at z_1, that sheath thickness grows like the root of voltage,

$$z_s - z_1 = K_z\sqrt{\phi_p - \phi_1}, \tag{16}$$

when $K_z = (2\alpha^2/\eta_s)^{1/2}$. Recall that in saturation, $\phi_1 \ll -1$, so the root will always be positive and dominated by ϕ_1.

Meanwhile, in the upstream region, where $\dot{\omega}$ is zero, the electric field is at its strongest. When $R_i z_1 \gg 1$, the $(\phi')^2$ and ϕ' terms dominate the ϕ'' term in (14). The remaining balance between convection and electrical conduction in the $0 < z < z_1$ region is a quadratic on ϕ' that is solved when

$$\phi' = \frac{R_i}{\tau} + A(z_0 - z)^{1/2}$$
$$\eta = -\alpha^2\phi'' = \frac{A\alpha^2}{2}(z_0 - z)^{-1/2}.$$

A and z_0 are merely adaptations of the integration constants from (14). For η to be piece-wise continuous at z_1, A is determined from the downstream solution,

$$A = \frac{\eta_s(z_0 - z_1)^{1/2}}{\alpha^2} \tag{17}$$

When the same continuity is enforced for ϕ', the z_0 constant may be determined.

$$z_0 = \frac{z_s + z_1}{2} - \frac{\alpha^2 R_i}{2\tau\eta_s}$$
$$= z_1 + \frac{1}{2}K_z(\phi_p - \phi_1)^{1/2} - \frac{\alpha^2 R_i}{2\tau\eta_s} \tag{18a}$$

Upon integrating ϕ' and enforcing continuity at z_1, one finally obtains a set of

formulae for ϕ and η in the region $0 < z < z_1$,

$$\phi = \frac{R_i}{\tau}(z - z_1) + \frac{4\eta_s}{3\alpha^2}[(z_0 - z_1)^2 - (z_0 - z_1)^{1/2}(z_0 - z)^{3/2}] + \phi_1 \tag{18b}$$

$$\eta = \eta_s \sqrt{\frac{z_0 - z_1}{z_0 - z}} \tag{18c}$$

The potential at the start of the formation region is related to the applied potential, ϕ_a, simply by substituting $z = 0$ in (18b).

$$\phi_a = -\frac{R_i}{\tau} z_1 + \frac{4\eta_s}{3\alpha^2}[(z_0 - z_1)^2 - (z_0 - z_1)^{1/2} {z_0}^{3/2}] + \phi_1 \tag{19}$$

$$\approx \phi_1 - \frac{R_i}{\tau} z_1 \tag{20}$$

The first term is dominant, which allows for a simple approximation. Unfortunately, the approximation is too imprecise to give good predictions, but it illustrates that there is a voltage penalty on the order of $R_i z_1/\tau$ incurred to force the positive ions against the flow through the upstream gap.

The current flowing through the sheath is most readily calculated at $z = z_1$ from the downstream solution, (15a), which will be valid even when $z_1 = 0$.

$$\begin{aligned} F_i(z_1) &= \eta - {R_i}^{-1}\eta' - \tau {R_i}^{-1}\eta\phi' \\ &= \eta_s - \dot{\omega}(z_s - z_1) \\ &= \eta_s - \dot{\omega} K_z \sqrt{\phi_p - \phi_1} \end{aligned} \tag{21}$$

Equations (15a), (15b), (16), (18b), (18c), and (18a) represent explicit solutions for the sheath in terms of the interface potential, $\phi(z_1) = \phi_1$. This model is implicit with respect to the applied potential, ϕ_a, which may be calculated from (19). For the cases when $z_1 = 0$, $\phi_1 = \phi_a$, the upstream solution may be ignored, and only the downstream solution in (15b), (15a), and (16) need be considered. The piece-wise predictions for η are shown as a dotted line in Figure 3 for the only saturated case shown in that figure. Predictions for current versus voltage will be addressed in the next section.

3.4. Downstream Sheath

Figure 4 shows the sheath at the downstream boundary (near $z = 1$). Unlike the upstream sheath, this sheath always exists regardless of the applied voltage, causing the plasma potential to rise from earth ground. This sheath model requires the consideration of three layers. In the distant plasma, the flow is dominated by recombination and convection over long length scales, up to a location we will name z_{d1}, where the electron concentration begins to drop precipitously. This continues in a narrow layer where the diffusion of electrons is strong, until the electron concentration drops to zero at location we will name z_{d2}. When the plasma potential is elevated by an applied potential at the upstream boundary, there is a third layer where the concentration of electrons is zero. Otherwise, the third layer collapses, and $z_{d2} = 1$.

The same diffusive layer existed in the upstream solution after z_s, but it was possible to ignore it since the sheath ion concentration could be calculated explicitly. In the downstream sheath, the ion concentration dips along with the electron concentration,

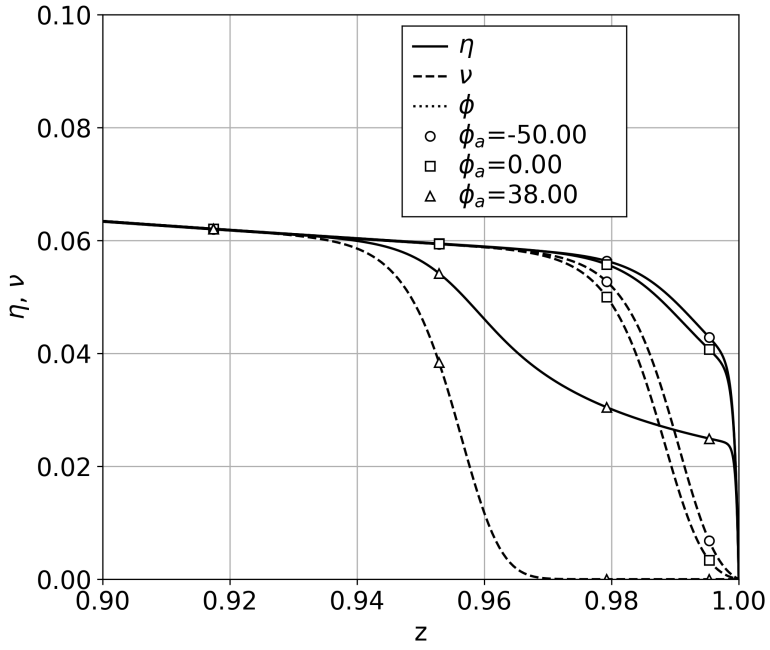

Figure 4. The sheaths at $z = 1$ from Figure 2.

and establishing a model for that dip is essential for predicting the sheath thickness and voltage drop.

However, if the purpose of the model is to predict the saturation current and its relationship to the applied voltage, then no such analysis is necessary. However thick the sheath is, and whatever electric field is incurred there, both the formation and depletion of ions will be zero or small. The sheath is evacuated of all electrons, so whatever electric current is observed at the downstream boundary will be due entirely to the positive ions that convected there from upstream. Therefore, in saturation everywhere in the downstream sheath will have ion flux density

$$F_i(z_{d2}) = \eta(z_{d2}). \tag{22}$$

As the electric field intensifies, ion transport in the sheath intensifies and their concentrations dip, but their flux density is conserved. All that remains is to predict the ion density delivered to the downstream sheath.

3.5. Bulk

In the bulk of the flow, far away from the sheaths, the length scales are on the order unity. The diffusion and mobility of positive ions here are too feeble to have any significant impact on the solution. Electrons are far more mobile, but they are forced to remain near their positive counterparts, so $\nu \approx \eta$. Therefore, the governing equations simplify dramatically.

$$0 = -\eta' - \beta\eta^2 + \dot{\omega} \tag{23}$$

These may be solved in a piece-wise fashion. In $z_1 < z < z_2$, $\dot{\omega}$ is a constant, and downstream of z_2, $\dot{\omega}$ is zero.

The boundary conditions are constructed by asserting that the ion concentration begins at zero and is piece-wise continuous at the interface between these regions.

$$\eta(z_1) = 0 \qquad\qquad \eta({z_2}^+) = \eta({z_2}^-) = \eta_2$$

Note that the peak ion concentration at the boundary, η_2 is defined here.

Were formation allowed to continue over an infinite length, the ion concentration would rise to bring formation into equilibrium with recombination, $\eta_\infty = \sqrt{\dot{\omega}/\beta}$. Using a slight variation on the solution of Bernoulli equations, when $\eta = y^{-1} + \eta_\infty$,

$$y' - 2\beta\eta_\infty y = \beta,$$

which is trivial to solve.

$$y = \begin{cases} A\exp(-2\sqrt{\dot{\omega}\beta}z) - \frac{1}{2\eta_\infty} & \dot{\omega} \neq 0 \\ \beta z + B & \dot{\omega} = 0 \end{cases}$$

Here, A and B are integration constants. When the boundary conditions are applied, solutions for η may be constructed.

$$\eta = \begin{cases} \eta_\infty - \frac{2\eta_\infty}{1+\exp\left(2\sqrt{\dot{\omega}\beta}(z-z_1)\right)} & z_1 < z < z_2 \\ \left({\eta_2}^{-1} + \beta(z-z_2)\right)^{-1} & z > z_2 \end{cases} \tag{24}$$

The peak ion concentration is

$$\eta_2 = \eta_\infty - \frac{2\eta_\infty}{1+\exp\left(2\sqrt{\dot{\omega}\beta}(z_2-z_1)\right)}, \tag{25}$$

and the ion concentration at the downstream boundary is

$$\eta_{d1} = \left({\eta_2}^{-1} + \beta(1-z_2)\right)^{-1}. \tag{26}$$

This solution is not plotted in Figure 2 because its curve is indistinguishable from the numerical results. Predictions for η_{d1} also reliably predict the saturation currents in the downstream sheath.

4. Results

4.1. Current-Voltage Characteristics

Figure 5 shows the IV characteristic for each of the five cases in Table 1. These are labelled by their type, lifted ($z_1 \neq 0$) or anchored ($z_1 = 0$); the length of the formation region, $L_f = z_2 - z_1$, and their Reynolds number, R. Lifted cases are plotted with filled markers while anchored cases are plotted with open markers.

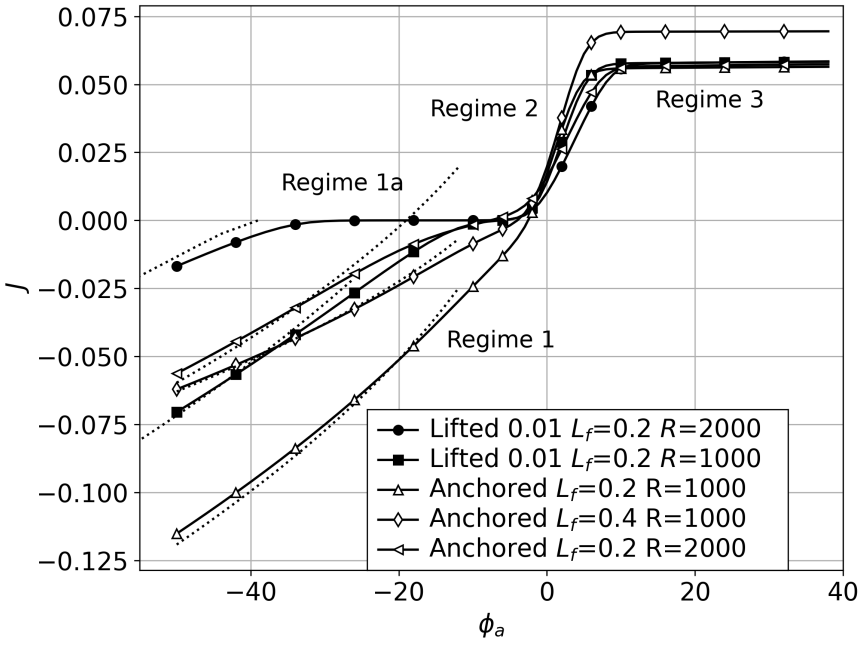

Figure 5. Current-voltage plots for the five cases. Asymptotic saturation solutions are shown with dotted lines. The regimes are annotated: (1) negative partial saturation, (1a) negative saturation, (2) unsaturated regime, (3) positive saturation.

The IV characteristic forms four regimes; one of which is not apparent in all cases. To remain consistent with the experimental works exploring these physics, we will label these:

Regime 1: Partial Saturation In the partial saturation mode, current is limited by the sheath at the upstream boundary, but the flow of current is still sensitive to voltage. In this mode, the gap between the formation region and the absorbing surface is small enough that the positive charge carrier's mobility allows it to be conducted. Meanwhile the flow of electrons has completely halted, so we elect to call this *partial* saturation: current limited absence of only one of the charge carriers but not the other.

The current predictions for the upstream saturation are plotted in dotted lines while assuming a plasma potential $\phi_p = 1$. The asymptotic solutions can be seen converging to the correct solution at large voltages and diverging somewhat at lower voltages, where accurate predictions for the plasma potential become important.

Regime 1a: Negative Saturation In negative saturation, the flow of all current halts because there is neither negative nor positive charge carriers in the upstream sheath. As is evident from Equation 21, promoting total saturation to partial saturation requires that the applied potential is high enough to overcome convection. This includes the penalty implied between ϕ_a and ϕ_1 due to a flame offset in Equation 19. When the applied potential is not sufficiently negative to enter regime 1 (when the current predicted by Equation 21 is positive), the system is, instead, in regime 1a. Regime 1a is especially interesting because it is occasionally absent. In anchored cases with small Reynolds numbers, it can be seen to be so small as to be undetectable.

Regime 2: Ohmic When neither the upstream nor the downstream sheath limits the flow of current, the limiting factor for the flow of current is the finite conductivity of the bulk of the plasma. In this narrow region, the current rapidly transitions between

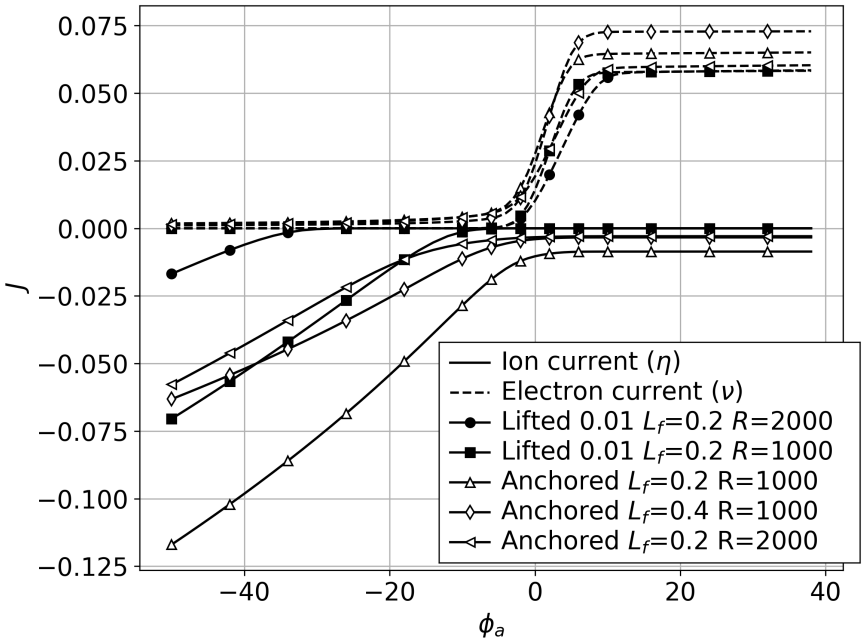

Figure 6. Electrical current due to positive ions and electrons at the upstream boundary. The currents in Figure 5 are the sum of the two curves shown here.

the two saturation regimes.

Regime 3: Positive Saturation Finally, when voltages are sufficiently positive to saturate the downstream sheath, all electrical current there is due to the delivery of positive charge due to convection. The further increase of voltage does nothing to enhance the delivery of charge. This is a true saturation.

4.2. Perturbation Solution

The local behavior of the IV characteristic operating in these different regimes is made clearer by examining the solution to the perturbation model in (11a), (11b), and (11c). Selected solutions are shown in Figure 7.

When the system experiences total saturation like in (b) and (d), the voltage change is absorbed entirely by growing one of the two sheaths. When the system is only partially saturated (in a), the majority of the voltage is absorbed in the upstream sheath, but the increase in current also incurs a voltage drop along the flame's length due to the finite conductivity of the flame. In the so-called "ohmic" regime, in (c), where the current in the flame was thought to be limited primarily by its electrical resistance, only roughly 30% of voltage changes are absorbed along the flame's length; the remaining 70% are split roughly evenly between the sheaths.

If the flame were truly in an "ohmic" mode of operation, the sheath voltage drops would be stable, and changes in the applied voltage would be absorbed entirely by changes in current through the finite resistance of the flame's bulk. When $R_i \gg 1$, the

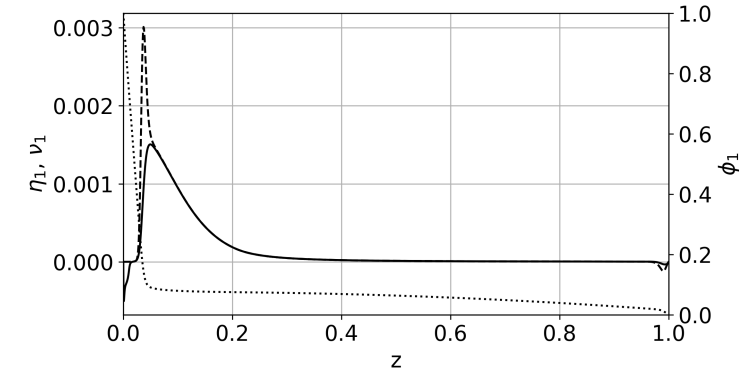

(a) Regime 1: $\phi_a = -50$

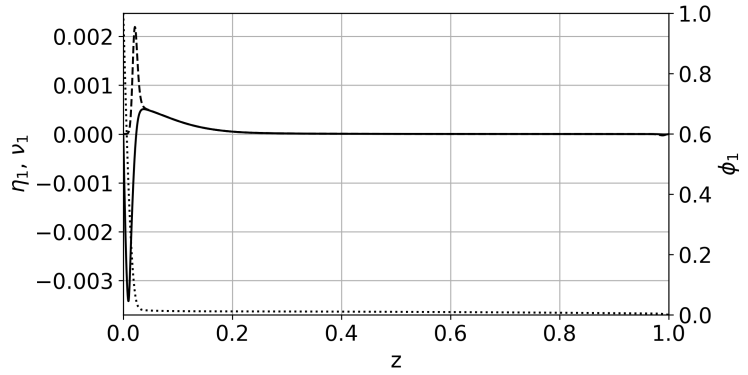

(b) Regime 1a: $\phi_a = -10$

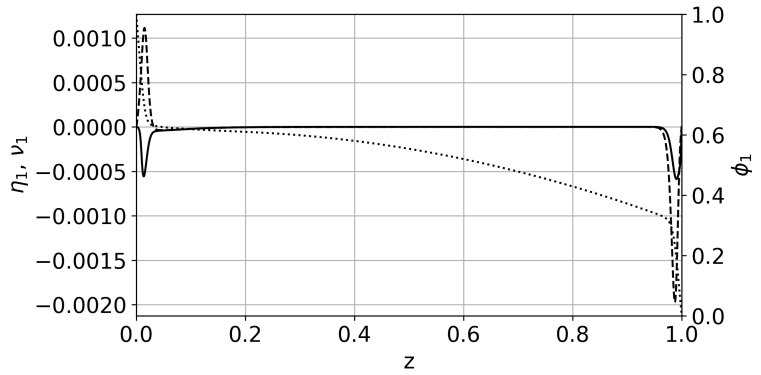

(c) Regime 2: $\phi_a = 2$

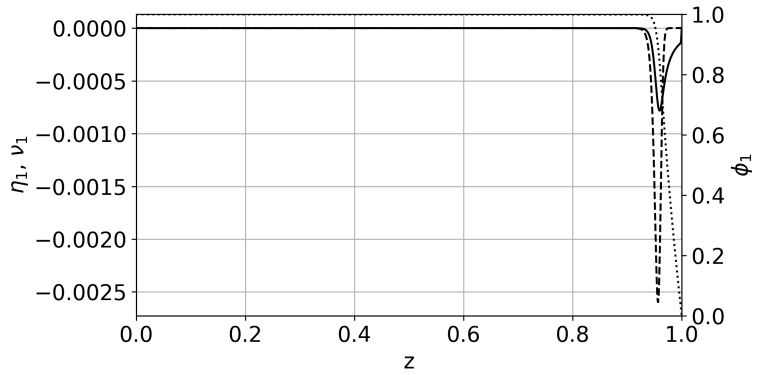

(d) Regime 3: $\phi_a = 38$

Figure 7. Sensitivity of the η (solid), ν (dashed), and ϕ (dotted) solutions per unit change in applied voltage, ϕ_a. The conditions are in (a) regime 1, (b) regime 1a, (c) regime 2, (d) regime 3.

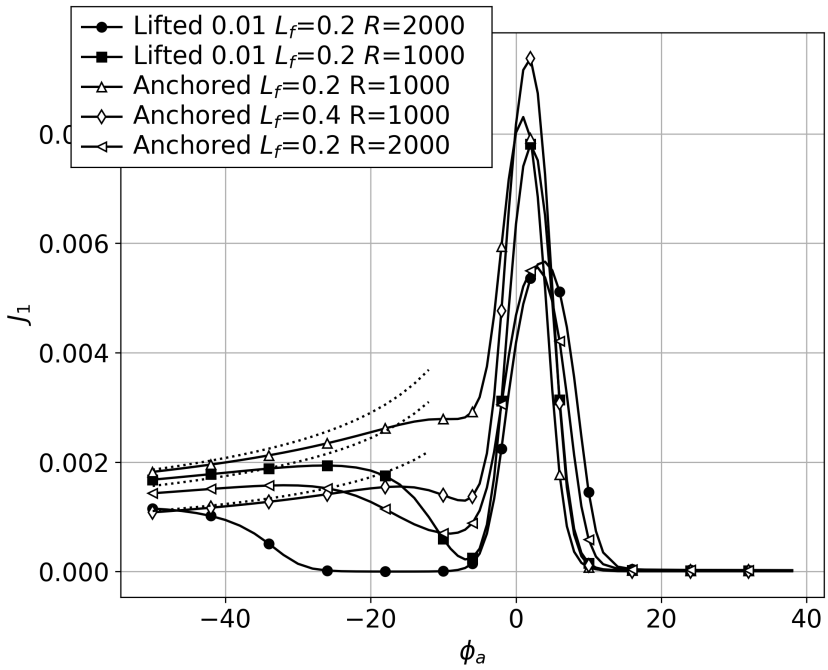

Figure 8. Flame conductance, J_1, versus applied voltage for the five cases.

increase in flame current per change in applied voltage in (12c) can be simplified to

$$\begin{aligned} J_1 &\approx \eta_1 - \nu_1 - {R_e}^{-1}[-\nu_1' + \nu_0\phi_1'] \\ &\approx -{R_e}^{-1}\nu_0\phi_1', \end{aligned} \tag{27}$$

when ν_1' is small over the domain. This is shown to be the case, since changes in the applied voltage over this range only impact the charge density at the sheaths, not in the bulk of the flame.

It is possible to calculate a simple estimate for flame resistance since, just like J, J_1 is a constant over the entire domain. Further, the integral of ϕ_1 is -1, due to the perturbation boundary conditions. Therefore, the flame conductivity is

$$J_1 \approx \frac{1}{R_e \int_0^1 {\nu_0}^{-1} \mathrm{d}z}, \tag{28}$$

and the flame's resistance is $R_e \int_0^1 {\nu_0}^{-1} \mathrm{d}z$. The electrical resistance is determined by the scarcity of electrons.

The actual flame conductance calculated for the model for the five cases is shown in Figure 8. Even if ν were at its minimum value (say about .06 for case 2) over the entire domain, the result would be roughly double the actual value shown in Figure 8. Clearly, (28) over-predicts conductance because the voltage drops at the sheaths have been neglected. In these cases, regime 2 is not truly ohmic.

5. Conclusions

A reduced-order, one-dimensional model for ion transport between upstream and downstream absorbing surfaces is presented with associated asymptotic solutions for the sheaths and the ion currents. Despite the appearance of an *apparently* linear regime between the saturation phenomena in the IV characteristic, the mode of conduction is never purely ohmic. At all conditions studied, the local IV characteristics of at least one of the sheaths plays a significant role in determining the current conducted by the flame.

5.1. Asymptotic Solutions

The upstream sheath ($z = 0$) asymptotic solution requires

- $\phi_1 < \phi_p - {\eta_s}^3/\dot{\omega}^2 {K_z}^2$: The voltage at the upstream edge of the formation region must be strong enough to overcome convection and drive current upstream. This is required for (21) to be negative.
- $\phi_a \ll \phi_p - {\eta_s}^3/\dot{\omega}^2 {K_z}^2 - R_i z_1/\tau$: To ensure the above condition, the applied voltage must be strong enough to drive a conductive bridge through the upstream gap. This is a combination of (21) and the approximation for (19).
- $R_i z_1 \gg 1$: The asymptotic analysis presumed that convection dominated diffusion in the upstream gap. For very thin gaps, the gap may merely be presumed zero, so $\phi_a = \phi_1$, and $z_1 \approx 0$.
- $R_i \gg R_e$: The mobility of the positive ions must far exceed the mobility of negative ions. This is required for the assumptions that negative particles evacuate the sheath *before* a conductive path is formed.

When these conditions are met, the model is biased in regime 1, and currents through the upstream sheath may be estimated by (21). In this mode of *partial* saturation, the upstream sheath has grown into the formation region, and a region of constant ion density forms there. The resulting bridge of positive ions between the formation region and the upstream boundary is the only remaining conductive path for electrical currents through the flame.

When $\phi_a \ll \phi_p$ but is insufficient to bias the system into regime 1, the model is biased in regime 1a, and currents are very nearly zero. In this mode, electrons have evacuated the region upstream of the ion formation region, but the applied potential is not yet sufficient to form a conductive path between the ion formation region and the upstream boundary. As a result, the flow of current is blocked.

The downstream sheath ($z = 1$) saturation currents are determined entirely by the ions that survive to impact the downstream surface, η_{d1}, calculated by (25) and (26),

$$\eta_\infty = \sqrt{\frac{\dot{\omega}}{\beta}} \qquad \eta_2 = \eta_\infty - \frac{2\eta_\infty}{1 + \exp\left(2\sqrt{\dot{\omega}\beta}(z_2 - z_1)\right)}$$

$$\frac{1}{\eta_{d1}} = \frac{1}{\eta_2} + \beta(1 - z_2)$$

This solution is valid when

- $\phi_a \gg \phi_p$: The applied voltage is sufficient to bias current positive.
- $R_i \gg R_e$: The mobility of negative charge carriers far exceeds the mobility of positive charge carriers.
- $\alpha \ll 1$: Electrical forces will mandate both charge carriers to share the same solution in the flame's bulk.
- $R_i \gg 1$: Diffusion and mobility of positive ions are not important in the flame's bulk.

When the electrical potential is positive, but so meager that the system is not in regime 3, then the model is biased in regime 2. Here, the flow of current is determined by a series of voltage drops incurred in each of the two sheaths and ohmic losses in the bulk of the flame. In this mode, the apparent conductance of the flame is at its maximum.

5.2. Comparison with Oxyfuel Experiments

The shapes of the model's predicted IV characteristics are astonishingly consistent with the shapes in Figure 1 and all other experiments in the oxyfuel flame. The model correctly predicts the existence of regime 1, and it correctly predicts that elongating the formation region suppresses regime 1 currents, as is seen in rich fuel/oxygen ratio tests exhibiting elongated inner cones. Measurements of regime 2 slope in the oxyfuel system have also confirmed that some degree of nonlinearity appears unless regime 3 currents are very high [25], supporting the finding that the system may not be truly ohmic.

Regime 1a has never been observed in the oxyfuel flame, but the transition from regime 1a to regime 1 has been identified in other flames as *super-saturation* [36]. Realistic estimates for Reynolds numbers in the oxyfuel flame are well in excess of 2000, so this model predicts that regime 1a should be present. It seems almost certain that this is due to the limitations implied by uniform velocity and 1D assumptions. In the oxyfuel flame, the shear layers at the torch tip will induce local velocities far below those estimated in the jets. This inspires the use of a local Reynolds number that more appropriately describes the balance between convection and electrical mobility in the space between the flame front and the torch tip. The quantity, $R_i z_1$, which appears in (19), already does this for the correct length scale, but for an unrealistically large velocity scale. It is for this reason that we have elected to examine results with Reynolds numbers far below what are typical in the bulk of the flame, which correctly predict the disappearance of regime 1a.

In agreement with many one-dimensional models and experiments (e.g. [35, 36, 29]), the present model predicts transition between regimes 1 and 2 at nearly zero current, but the oxyfuel flame demonstrates a significant current offset that is variable with operating conditions [21]. Just as with the absence of regime 1a, this is likely due to aspects of a geometrically complex system that defy such a simple model. For example, if recirculation were to impose a negative local velocity, that could drive the kind of negative current offset observed in Figure 1.

The model predicts roughly 0.06 regime 3 saturation current. If the flame were a cylinder with diameter 6mm, velocity 100m/s, and number density scale $3 \times 10^{18}\mathrm{m}^{-3}$ [23], the $J = 0.06$ scales to roughly 80μA, which gives order-of-magnitude agreement with measurements in the oxyfuel flame [22] with no particular care taken to tune the model to match experiment. While the model predicts a nearly flat regime 3 current, the oxyfuel flame shows a persistent climb. The stagnation at the work surface

suppresses the local axial velocity there, so the recombination length scales (β^{-1}) there will be compressed. If the model were configured with a shorter recombination length (lower velocity, larger β) such that the ion concentration were to decline far more rapidly in the immediate vicinity of the downstream boundary, applying higher potentials to cause the downstream sheath to reach deeper into the flow would enhance the regime 3 saturation current far more than what is observed here. Instead, the uniform velocity model may be more appropriate to the metal screens often used for downstream boundaries in flat burner-stabilized experiments.

Figure 8 shows a regime 2 conductivity on the order .008, which if the flame were a cylinder with diameter 6mm, velocity 100m/s, and number density scale $3 \times 10^{18}\mathrm{m}^{-3}$, corresponds to an electrical resistance of approximately 150kΩ. This coincides astonishingly well with direct measurements of the oxyfuel flame regime 2 resistance [22, fig.5]. We have now provided two re-scaled result comparisons against experiment that seem to agree quite well, but great care should be taken interpreting this apparent success before a more rigorous re-scaling study can be conducted. Instead, this effort has been scoped to the derivation, solution, and study of the model's features.

Acknowledgments

This material is based upon work supported by the National Science Foundation under Grant No. 1900698.

References

[1] H. Banta. The mobility of positive ions in flames. *Physical Review*, 33, February 1929.

[2] Memdouh Belhi, Pascale Domingo, and Pierre Vervisch. Direct numerical simulation of the effect of an electric field on flame stability. *Combustion and Flame*, 157:2286–2297, 2010.

[3] Memdouh Belhi, Bok Jik Lee, Min Suk Cha, and Hong G. Im. Three-dimensional simulation of ionic wind in a laminar premixed Bunsen flame subjected to a traverse dc electric field. *Combustion and Flame*, 202:90–106, 2019.

[4] Paul E. Boucher. The drop of potential at the cathode in flames. *Physical Review*, 31, May 1928.

[5] H. F. Calcote. Ion production and recombination in flames. In *Eighth Symposium on Combustion*, volume 8, pages 184–199. Combustion Institute, 1961.

[6] Yu-Chien Chien, David Escofet-Martin, and Derek Dunn-Rankin. Ion current and carbon monoxide release from an impinging methane/air coflow flame in an electric field. *Combustion and Flame*, 204:250–259, 2019.

[7] B. T. Chorpening, J. D. Thornton, E. D. Huckaby, and K. J. Benson. Combustion oscillation monitoring using flame ionization in a turbulent premixed combustor. In *Proceedings of the ASME*, volume 129, pages 352–357, 2007.

[8] R. M. Clements and P. R. Smy. Electrostatic-probe studies in a flame plasma. *Journal of Applied Physics*, 40:4553–4558, 1969.

[9] R. M. Clements and P. R. Smy. Ion current from a collision-dominated flowing plasma to a cylindrical electrode surrounded by a thin sheath. *Journal of Applied Physics*, 41(9):3745–3749, 1970.

[10] R. M. Clements and P. R. Smy. Ion current to a spherical probe in a flowing high-pressure plasma under thin-sheath conditions. *Proceedings of the IEE*, 117(8):1721–1724, 1970.

[11] R. M. Clements and P. R. Smy. Ion saturation currents to planar langmuir probes in a collision-dominated flowing plasma. *Journal of Physics D: Applied Physics*, 6:184–195, 1973.

[12] Alexander B. Fialkov. Investigations on ions in flames. *Progress in Energy and Combustion Science*, 23:399–528, 1997.

[13] Jie Han, Memdouh Belhi, Tiernan Casey, Fabrizio Bisetti, Hong Im, and Jyh-Yuan Chen. The i-v curve characteristics of burner-stabilized premixed flames: detailed and reduced models. In *Proceedings of the Combustion Institute*, volume 36, pages 1241–1250, 2017.

[14] N. Henein, W. Bryzik, A. Abdel-Rehim, and A. Gupta. Characteristics of ion current signals in compression ignition and spark ignition engines. *SAE International Journal of Engines*, 3(1):260–281, April 2010.

[15] Torkil Holm. Aspects of the mechanism of the flame ionization detector. *Journal of Chromatography A*, 842:221–227, 1999.

[16] A.R. Jones. Flame failure detection and modern boilers. *Journal of Physics E: Scientific Instruments*, 21:921–928, 1988.

[17] Maxime Karrer, Marc Bellenoue, Sergei Labuda, Julien Sotton, and Maxime Makarov. Electrical probe diagnostics for the laminar flame quenching distance. *Experimental Thermal and Fluid Science*, 34:131–141, 2010.

[18] Irving Langmuir. Studies of electric discharges in gases at low pressures. *General Electric Review*, 27(12):810, 1924.

[19] Fangyan Li, Lijun Xu, Minglong Du, Lijun Yang, and Zhang Cao. Ion current sensing-based lean blowout detection for a pulse combustor. *Combustion and Flame*, 176:263–271, 2017.

[20] S.D. Marcum and B.N. Ganguly. Electric-field-induced flame speed modification. *Combustion and Flame*, 143:27–36, 2005.

[21] Christopher Martin, Castle Leonard, and Josh VonFricken. A study of the electrical characteristics of an oxy-fuel flame. *Experimental Thermal and Fluid Science*, 88:65–72, 2017.

[22] Christopher R. Martin. A study of ion currents in an oxyfuel flame due to work surface chemical action. *Experimental Thermal and Fluid Science*, 98:239–250, 2018.

[23] Christopher R. Martin, Alex Untaroiu, and Kemu Xu. Spatially resolved ion density measurements in an oxyfuel cutting flame. *Combustion Science and Technology*, 2020. [Submitted].

[24] Luck B.W. Peerlings, Manohar, Viktor N. Komilov, and Philip de Goey. Flame ion generation rate as a measure of the flame thermo-acoustic response. *Combustion and Flame*, 160:2490–2496, 2013.

[25] Teresa L. Pond and Christopher R. Martin. Electrical characteristics of the oxyfuel flame while cutting steel. *Experimental Thermal and Fluid Science*, 112, 2020.

[26] Rahul Rao and Damon Honnery. A simplified mechanism for the prediction of the ion current during methane oxidation in engine-like conditions. *Combustion and Flame*, 162:2928 – 2936, 2015.

[27] Rahul Rao and Damon Honnery. A study of the relationship between NOx and the ion current in a direct-injection diesel engine. *Combustion and Flame*, 176:309–317, 2017.

[28] M. Di Renzo, P. De Palma, M. D. de Tullio, and G. Pascazio. An efficient flamelet progress-variable method for modeling non-premixed flames in weak electric fields. *Computers and Fluids*, 157:14–27, 2017.

[29] N. Speelman, L.P.H. de Goey, and J.A. van Oijen. Development of a numerical model for the electric current in burner-stabilised methane-air flames. *Combustion Theory and Modeling*, 19(2):159–187, 2015.

[30] N. Speelman, M. Kiefer, D. Markus, U. Maas, L.P.H. de Goey, and J.A. van Oijen. Validation of a novel numerical model for the electrical currents in burner-stabilized methane-air flames. In *Proceedings of the Combustion Institute*, volume 35, pages 847–854, 2015.

[31] C. H. Su and S. H. Lam. Continuum theory of spherical electrostatic probes. *The Physics of Fluids*, 6(10), October 1963.

[32] Jesse Tinajero and Derek Dunn-Rankin. Non-premixed axisymmetric flames driven by ion currents. *Combustion and Flame*, 199:365–376, 2019.

[33] J.D.B.J. van den Boom, A.A. Konnov, A.M.H.H. Verhasselt, V.N. Kornilov, L.P.H. de Goey, and H. Nijmeijer. The effect of a DC electric field on the laminar burning velocity of premixed methane/air flames. In *Proceedings of the Combustion Institute*, volume 32, pages 1237–1244, 2009.

[34] F.J. Weinberg, D. Dunn-Rankin, F.B. Carleton, S. Karnani, C. Markides, and M. Zhai. Electrical aspects of flame quenching. In *Proceedings of the Combustion Institute*, volume 34, pages 3295–3301, 2013.

[35] Y. Xiong, D. G. Park, L. Bok Jik, C. Suk Ho, and C. Min Suk. Dc field response of one-dimensional flames using an ionized layer model. *Combustion and Flame*, 163:317–325, 2016.

[36] Kiyotaka Yamashita, Sunny Karnani, and Derek Dunn-Rankin. Numerical prediction of ion current form a small methane jet flame. *Combustion and Flame*, 156:1227–1233, 2009.